



# ImmunoPET of Ovarian and Pancreatic Cancer with AR9.6, a Novel MUC16-Targeted Therapeutic Antibody

Sai Kiran Sharma<sup>1</sup>, Kyea N. Mack<sup>1,2,3</sup>, Alessandra Piersigilli<sup>4</sup>, Jacob Pourat<sup>1</sup>, Kimberly J. Edwards<sup>1</sup>, Outi Keinänen<sup>1,5</sup>, Maria S. Jiao<sup>4</sup>, Huiyong Zhao<sup>6</sup>, Brandy White<sup>7</sup>, Cory L. Brooks<sup>7</sup>, Elisa de Stanchina<sup>6</sup>, Madi R. Madiyalakan<sup>8</sup>, Michael A. Hollingsworth<sup>9</sup>, Prakash Radhakrishnan<sup>9</sup>, Jason S. Lewis<sup>1,3,10,11</sup>, and Brian M. Zeglis<sup>1,5,10,12,13</sup>

## ABSTRACT

**Purpose:** Advances in our understanding of the contribution of aberrant glycosylation to the pro-oncogenic signaling and metastasis of tumor cells have reinvigorated the development of mucin-targeted therapies. Here, we validate the tumor-targeting ability of a novel monoclonal antibody (mAb), AR9.6, that binds MUC16 and abrogates downstream oncogenic signaling to confer a therapeutic response.

**Experimental Design:** The *in vitro* and *ex vivo* validation of the binding of AR9.6 to MUC16 was achieved via flow cytometry, radioligand binding assay (RBA), and immunohistochemistry (IHC). The *in vivo* MUC16 targeting of AR9.6 was validated by creating a <sup>89</sup>Zr-labeled radioimmunoconjugate of the mAb and utilizing immunoPET and *ex vivo* biodistribution studies in xenograft models of human ovarian and pancreatic cancer.

**Results:** Flow cytometry, RBA, and IHC revealed that AR9.6 binds to ovarian and pancreatic cancer cells in an MUC16-depen-

dent manner. The *in vivo* radiopharmacologic profile of <sup>89</sup>Zr-labeled AR9.6 in mice bearing ovarian and pancreatic cancer xenografts confirmed the MUC16-dependent tumor targeting by the radioimmunoconjugate. Radioactivity uptake was also observed in the distant lymph nodes (LNs) of mice bearing xenografts with high levels of MUC16 expression (i.e., OVCAR3 and Capan-2). IHC analyses of these PET-positive LNs highlighted the presence of shed antigen as well as necrotic, phagocytized, and actively infiltrating neoplastic cells. The humanization of AR9.6 did not compromise its ability to target MUC16-expressing tumors.

**Conclusions:** The unique therapeutic mechanism of AR9.6 combined with its excellent *in vivo* tumor targeting makes it a highly promising theranostic agent. huAR9.6 is poised for clinical translation to impact the management of metastatic ovarian and pancreatic cancers.

## Introduction

Cancers of the pancreas and ovaries rank among the top five leading causes of cancer-related deaths in the United States (1). Although localized forms of these malignancies are treated with surgery and adjuvant chemotherapy, there is an unmet clinical need for more effective targeted therapies for patients with metastatic disease (2, 3). The growing appreciation for the role of altered glycosylation in cancer progression has uncovered aberrantly glycosylated proteins as a promising druggable target (4). Along these lines, particular attention has been paid to epithelial cell-surface glycoproteins called mucins (5). Although mucins primarily serve to form as a barrier that protects epithelial cells from mechanical forces and infection, altered glycoforms of mucins expressed by transformed cells have been implicated in the induction of oncogenic features and the orchestration of the metastatic potential of cancer cells (6, 7). Mucin-16 (MUC16) ranks among the most widely known mucins due to the utility of its CA125 epitope as a biomarker for serous ovarian cancer (8). Isoforms of MUC16 have also been implicated in the progression and metastasis of pancreatic ductal adenocarcinoma as well as aggressive subtypes of the disease such as squamous and basal-like carcinomas (9, 10). Despite its endogenous expression in a few healthy tissues and status as a shed antigen, MUC16 remains a viable therapeutic target for antibody-based and adoptive cell therapies (11–19).

The majority of MUC16-targeted antibodies bind CA125 epitopes in the SEA/tandem repeat region (10, 20) or the unshed carboxy-terminus domain (13, 21, 22). To date, anti-MUC16 antibodies have mostly been harnessed as vectors to deliver toxic payloads, radionuclides, or fluorophores (12, 23–26). More recently,

<sup>1</sup>Department of Radiology, Memorial Sloan Kettering Cancer Center, New York, New York. <sup>2</sup>Department of Pharmacology, Weill Cornell Medical College, New York, New York. <sup>3</sup>Molecular Pharmacology Program, Memorial Sloan Kettering Cancer Center, New York, New York. <sup>4</sup>Tri-Institutional Laboratory of Comparative Pathology, Memorial Sloan Kettering Cancer Center, Weill Cornell Medical College, and The Rockefeller University, New York. <sup>5</sup>Department of Chemistry, Hunter College, City University of New York, New York, New York. <sup>6</sup>Anti-Tumor Assessment Core, Memorial Sloan Kettering Cancer Center, New York. <sup>7</sup>Department of Chemistry, California State University, Fresno, California. <sup>8</sup>Quest PharmaTech Inc., Edmonton, AB, Canada. <sup>9</sup>Eppley Institute for Research in Cancer and Allied Diseases, Fred and Pamela Buffett Cancer Center, University of Nebraska Medical Center, Omaha, Nebraska. <sup>10</sup>Department of Radiology, Weill Cornell Medical College, New York, New York. <sup>11</sup>Radiochemistry and Molecular Imaging Probes Core, Memorial Sloan Kettering Cancer Center, New York, New York. <sup>12</sup>Ph.D. Program in Chemistry, The Graduate Center of the City University of New York, New York, New York. <sup>13</sup>Ph.D. Program in Biochemistry, The Graduate Center of the City University of New York, New York, New York.

**Note:** Supplementary data for this article are available at Clinical Cancer Research Online (<http://clincancerres.aacrjournals.org/>).

**Corresponding Authors:** Brian M. Zeglis, Department of Chemistry, Hunter College, 413 East 69th Street, New York, NY 10021. Phone: 212-896-0433; E-mail: bz102@hunter.cuny.edu; and Jason S. Lewis, 1275 York Avenue, New York, NY 10065. Phone: 646-888-3038; E-mail: lewisj2@mskcc.org

Clin Cancer Res 2022;28:948–59

doi: 10.1158/1078-0432.CCR-21-1798

This open access article is distributed under Creative Commons Attribution-NonCommercial-NoDerivatives License 4.0 International (CC BY-NC-ND).

©2021 The Authors; Published by the American Association for Cancer Research

### Translational Relevance

In recent years, proteins with aberrant glycosylation patterns have emerged as therapeutic targets in oncology. Along these lines, MUC16 glycoforms have been implicated in the oncogenesis and metastatic progression of high-grade serous ovarian cancer and pancreatic ductal adenocarcinoma. AR9.6 is a therapeutic mAb that binds to MUC16, interferes with the interaction of MUC16 with ErbB receptors on the surface of cancer cells, and thereby attenuates the activation of downstream oncogenic signaling pathways. Here, we report the *in vitro*, *ex vivo*, and *in vivo* validation of [<sup>89</sup>Zr]Zr-DFO-muAR9.6 and [<sup>89</sup>Zr]Zr-DFO-huAR9.6 in murine models of MUC16-positive high-grade serous ovarian cancer and pancreatic ductal adenocarcinoma. Both radioimmunoconjugates displayed excellent tumor-targeting properties *in vivo*, ultimately producing high-quality PET images. This suggests that [<sup>89</sup>Zr]Zr-DFO-huAR9.6 could play essential roles in the clinic as a theranostic imaging agent for AR9.6 therapy and as a tool for the preoperative delineation of draining or metastatic lymph nodes.

a new class of MUC16-targeted antibodies that interact with the N- or O-glycosylation sites on MUC16 has emerged and exert a therapeutic effect by abrogating the downstream pro-oncogenic signaling of cancer cells (10, 15). AR9.6 is one such mAb, as it binds to SEA domain 5 on MUC16 and interferes with the interaction of MUC16 with ErbB (EGF) receptors on the cancer cell surface. The latter attenuates the subsequent activation of oncogenic AKT and GSK3 $\beta$  signaling pathways in tumor cells (10).

Herein, we describe the *in vitro*, *in vivo*, and *ex vivo* validation of AR9.6 binding to MUC16 in xenograft models of human ovarian and pancreatic cancers. Furthermore, we functionally validate a humanized version of AR9.6 (huAR9.6) in anticipation of its clinical use as a theranostic agent for the noninvasive delineation and treatment of metastatic ovarian and pancreatic cancers.

## Materials and Methods

Detailed experimental procedures can be found in Supporting Information.

### Ovarian and pancreatic cancer cell lines

Human ovarian adenocarcinoma OVCAR3 and SKOV3 cells were purchased from American Type Culture Collection (ATCC) in 2013. Both cell lines were used for implanting tumors in mice between passages 3 and 6 after the first thaw of the source vial. Human pancreatic ductal adenocarcinoma (PDAC) cell lines Capan-2, BxPC-3, and MIAPaCa-2 were purchased from ATCC in 2014–2015 and used for implanting tumors in mice between passages 3 and 6 after the first thaw of the source vial. S2-028 and T3M-4 cell lines were provided by the laboratory of Dr. Hollingsworth at the University of Nebraska Medical Center (UNMC) and used between passages 40 and 50 for implanting tumors in mice. In addition to routine testing for *mycoplasma* using the Lonza MycoAlert mycoplasma detection kit (LT07-418), all cell lines were authenticated by STR profiling at MSKCC and UNMC repeatedly between 2009 and 2018. Ovarian cancer patient-derived xenograft (PDX) lines OvCa PDX0003, PDX0004, and PDX0012 were obtained via IRB approval and maintained by the antitumor assessment core at MSKCC, sequenced via Integrated Mutation Profiling

for Actionable Cancer Targets (IMPACT), and used at passage 4 for the studies described herein.

### muAR9.6 expression and purification

The hybridoma for murine AR9.6 (muAR9.6) production was provided by Dr. Madi Madiyalakan (Quest PharmaTech Inc.), Dr. Prakash Radhakrishnan, and Dr. Michael Hollingsworth (UNMC). muAR9.6 was purified from hybridoma cell culture supernatant using protein G affinity chromatography.

### Bioconjugation and radiolabeling

<sup>89</sup>Zr-labeled muAR9.6 and huAR9.6 were prepared using established procedures (27). Briefly, the [<sup>89</sup>Zr]Zr<sup>4+</sup> chelator desferrioxamine (DFO) was attached to the antibody by reacting 3 mg of AR9.6 antibody (>2 mg/mL) with 10 molar equivalents of *p*-SCN-DFO (B-705; Macrocyclics, Inc.). Zirconium-89 ([<sup>89</sup>Zr]Zr-oxalate) was procured from 3D Imaging or produced at Memorial Sloan Kettering Cancer Center on a TR19/9 cyclotron (Ebco Industries Inc.). During radiolabeling, <sup>89</sup>Zr[Zr]-oxalate was neutralized using 1 M sodium carbonate, and—depending on the scale of the study—<sup>89</sup>Zr-labeled radioimmunoconjugates were prepared by mixing 41 to 163 MBq (1.1–4.4 mCi) of pH-adjusted <sup>89</sup>Zr[Zr]<sup>4+</sup> with 150 to 870  $\mu$ g of DFO-AR9.6 in Chelex-treated PBS (pH 7.2) while achieving a radioactivity concentration between 2.5 and 9.0  $\mu$ Ci/ $\mu$ L.

### Xenograft models

All *in vivo* experiments described herein were approved by the Research Animal Resource Center and Institutional Animal Care and Use Committee (IACUC 08-07-013) of Memorial Sloan Kettering Cancer Center. Three types of animal models were used in this study: (i) mice bearing subcutaneous ovarian and pancreatic cancer cell line xenografts; (ii) mice bearing orthotopic ovarian and pancreatic cancer cell line xenografts; and (iii) mice bearing subcutaneous ovarian cancer PDX.

Eight- to 10-week-old Nu/Nu (CRL:NU-Foxn1<sup>tmu</sup>) female mice were purchased from Charles River Laboratories. Animals were housed in ventilated cages, given food and water ad libitum, and were allowed to acclimatize for 1 week prior to inoculation of tumor cells. Subcutaneous OVCAR3 and SKOV3 tumors were induced between the right shoulder and the liver by injection of 10 million and 5 million cells, respectively, in a 150- $\mu$ L cell suspension of a 1:1 (v/v) mixture of fresh media/BD Matrigel (BD Biosciences). To generate PDX models, patient tumor tissue that was not needed for diagnosis was collected under an approved IRB protocol and implanted subcutaneously into 6-week-old nod-scid-gamma (NSG) mice (005557; The Jackson Laboratory). Upon reaching the predetermined endpoint of 1,000 mm<sup>3</sup>, the tumor was processed to generate a single-cell suspension using the Gentlemacs kit (Miltenyi), as previously described (28). Five million cells of each of the OvCa PDX lines (012, 0004, and 0003) were implanted subcutaneously in the region between the right shoulder and liver of 6- to 8-week-old female NSG mice. Subcutaneous ovarian cancer xenografts were used for *in vivo* studies when the tumor volumes reached ~150 to 300 mm<sup>3</sup>. Orthotopic ovarian xenografts were developed by surgical implantation of  $1.0 \times 10^6$  OVCAR3 cells in the left ovary of 10-week-old female Nu/Nu mice according to published protocols (29). Orthotopic OVCAR3 xenografts were used for *in vivo* PET imaging 6 weeks after surgical implantation of tumor cells in the ovarian bursa.

Subcutaneous PDAC xenografts were generated by injection of 5 million cells of five cell lines—S2-028, Capan-2, T3M-4, BxPC-3, and

MIAPaCa-2—which were separately resuspended in a 150- $\mu$ L cell suspension of a 1:1 (v/v) mixture of fresh media/BD Matrigel (BD Biosciences) and implanted on the right flank of 6- to 8-week-old female Nu/Nu mice. Subcutaneous ovarian cancer xenografts were used for *in vivo* studies when the tumor volumes reached  $\sim 150$  to  $200\text{ mm}^3$ . Orthotopic pancreatic cancer xenografts were developed by surgical implantation of  $0.1 \times 10^6$  luciferase-transfected Capan-2 tumor cells into the head of the pancreas of 6-week-old female Nu/Nu mice according to published protocols (29). Orthotopic Luc-Capan-2 tumors were monitored by bioluminescence imaging (BLI) to assess tumor take prior to being used for terminal *in vivo* PET imaging at 4 weeks after surgical implantation of tumor cells into the head of the pancreas.

### PET imaging

PET-CT images were acquired on an Inveon PET-CT scanner (Siemens Healthcare). Tumor-bearing mice were administered  $238 \pm 24.6\text{ }\mu\text{Ci}$  ( $8.8 \pm 0.9\text{ MBq}$ ;  $41 \pm 16\text{ }\mu\text{g}$ ) of the  $^{89}\text{Zr}$ -labeled AR9.6 antibodies suspended in  $150\text{ }\mu\text{L}$  of PBS via the lateral tail vein. Single mouse PET-CT data were analyzed using Asipro image analysis software. Data acquired using the mouse “hotel” were calibrated and cropped before analysis on AMIDE software (Stanford University) and rendered for presentation using VivoQuant (Invivo).

### Ex vivo biodistribution

*Ex vivo* biodistribution analyses were performed in separate cohorts of xenograft mice that were administered  $26.3 \pm 2.7\text{ }\mu\text{Ci}$  ( $0.97 \pm 0.1\text{ MBq}$ ;  $4.9 \pm 1.7\text{ }\mu\text{g}$ ) of the  $^{89}\text{Zr}$ -labeled AR9.6 antibodies suspended in  $150\text{ }\mu\text{L}$  of PBS per mouse via the lateral tail vein. In blockade cohorts designed to validate binding specificity, mice were injected with a mixture of  $^{89}\text{Zr}$ -labeled AR9.6 and a 100-fold excess (mass) of unmodified and unlabeled AR9.6.

### Histopathology

Tissue samples harvested from PET-positive mice were fixed in 10% neutral buffered formalin. A period of 10 half-lives of Zr-89 ( $\sim 33$  days total) was allowed to pass before processing the samples for histopathologic analysis. Paraffin-embedded blocks were sliced to obtain  $5\text{-}\mu\text{m}$ -thick sections, and slides were stained with hematoxylin and eosin (H&E) and IHC. IHC staining of cryosections of ovarian patient tumors was done using muAR9.6 as the primary antibody at 1:100 dilution and a biotinylated goat anti-mouse (H + L) secondary antibody (BP-9200; Vector Labs) at 1:500 dilution. IHC staining of OVCAR3 tumors and lymph node sections was performed using huAR9.6 as the primary antibody at 1:100 dilution and a biotinylated goat anti-human (H + L) secondary antibody (BA-3000; Vector Labs) at 1:500 dilution. Pan-cytokeratin staining of sections from OVCAR3 tumors and lymph nodes was performed using a rabbit polyclonal antibody (Z0622; Dako) as the primary antibody and a biotinylated anti-rabbit IgG (H + L; PK-6100; Vector Labs) as the secondary antibody—both used at 1:500 dilution. Histopathologic analysis was performed in a blinded manner by a board-certified veterinary pathologist (AP).

### Humanization of muAR9.6

muAR9.6 was humanized using a human germline CDR grafting approach (30). Recombinant humanized AR9.6 (huAR9.6) was produced by transient transfection in expiCHO cells according to the manufacturer's instructions (Thermo Fisher Scientific). Transfections were carried out using a 2:1 ratio of light-chain to heavy-chain plasmids. The culture supernatant was harvested seven days after

transfection, and the antibody was purified using protein A affinity chromatography.

### Statistical analysis

All data are expressed as mean  $\pm$  standard deviation (SD). Statistical analysis was performed using GraphPad Prism version 9.1.0. Statistical comparisons of radioactivity concentrations in a given organ across groups in the *ex vivo* biodistribution studies were done using non-parametric multiple Mann-Whitney tests to compare ranks. The Holm-Sidak multiple comparison test was applied, and the threshold for *P* value comparison was set to 0.05.

## Results

### In vitro and in vivo characterization of muAR9.6

FPLC purification using protein G affinity chromatography yielded  $\sim 25\text{ mg/L}$  of muAR9.6 (IgG1-kappa) having  $\geq 95\%$  monomeric content from hybridoma culture supernatant (Supplementary Fig. S1 and S2). Flow cytometry of the unmodified muAR9.6 revealed strong binding to OVCAR3 cells, a cell line representative of high-grade serous ovarian cancer that is known to express high levels of MUC16 (Fig. 1A). In contrast, muAR9.6 exhibited marginal binding to SKOV3 cells, a cell line representative of clear cell ovarian carcinoma that is considered to be MUC16 negative yet exhibits low levels of MUC16 expression (Figure 1B; Supplementary Fig. S3). The labeling of DFO-modified muAR9.6 with Zr-89 produced a radioimmunoconjugate— $^{89}\text{Zr}$ [Zr]-DFO-muAR9.6—with high specific activity (5–10 mCi/mg) and radiochemical stability (Supplementary Fig. S4–S6). The binding of  $^{89}\text{Zr}$ [Zr]-DFO-muAR9.6 to OVCAR3 cells was found to be  $\sim 4\times$  greater than that to SKOV3 cells, and—importantly—the binding of the radioimmunoconjugate to the antigen-positive cells could be blocked by a 100-fold excess of unlabeled muAR9.6 (Fig. 1C). Furthermore, immunostaining and fluorescence microscopy confirmed that both muAR9.6 and FITC-modified muAR9.6 bind to the membrane of MUC16-expressing OVCAR3 cells (Fig. 1D).

With this *in vitro* characterization complete, we next interrogated the *in vivo* behavior of  $^{89}\text{Zr}$ [Zr]-DFO-muAR9.6 in mice bearing subcutaneous OVCAR3 and SKOV3 xenografts. ImmunoPET with  $^{89}\text{Zr}$ [Zr]-DFO-muAR9.6 revealed high uptake of the radioimmunoconjugate in OVCAR3 tumors ( $\sim 35\%$ ID/g), producing high-contrast PET images (Fig. 1E; Supplementary Fig. S7). In contrast, analogous experiments in the mice bearing SKOV3 xenografts displayed lower amounts of  $^{89}\text{Zr}$ [Zr]-DFO-muAR9.6 in tumor tissue ( $\sim 17\%$ ID/g), likely a result of the enhanced permeability and retention effect and low levels of antigen expression—as well as with higher activity concentrations in the blood and liver (Fig. 1E; Supplementary Fig. S8). Intriguingly, the *ex vivo* biodistribution analysis of  $^{89}\text{Zr}$ [Zr]-DFO-muAR9.6 in mice with OVCAR3 xenografts demonstrated heterogeneous radioactivity concentrations in the blood, liver, and tumor. Specifically, animals with high uptake in the liver exhibited low radioactivity concentration in the blood as early as 1 day postinjection (p.i.). This somewhat unusual phenomenon was encountered in three independent biodistribution experiments. Nonetheless, over the course of the experiment, radioactivity concentrations in the OVCAR3 tumors increased (from  $12.0 \pm 2.6\%$ ID/g at 1 d p.i. to  $33.4 \pm 3.5\%$ ID/g at 5 d p.i.), while those in the blood decreased over the same period (from  $9.6 \pm 4.1\%$ ID/g at 1 d p.i. to  $2.9 \pm 1.7\%$ ID/g at 5 d p.i.) (Fig. 1F; Supplementary Table S1).

Mice bearing OVCAR3 xenografts coinjected with a 100-fold excess of unlabeled muAR9.6 alongside  $^{89}\text{Zr}$ [Zr]-DFO-muAR9.6

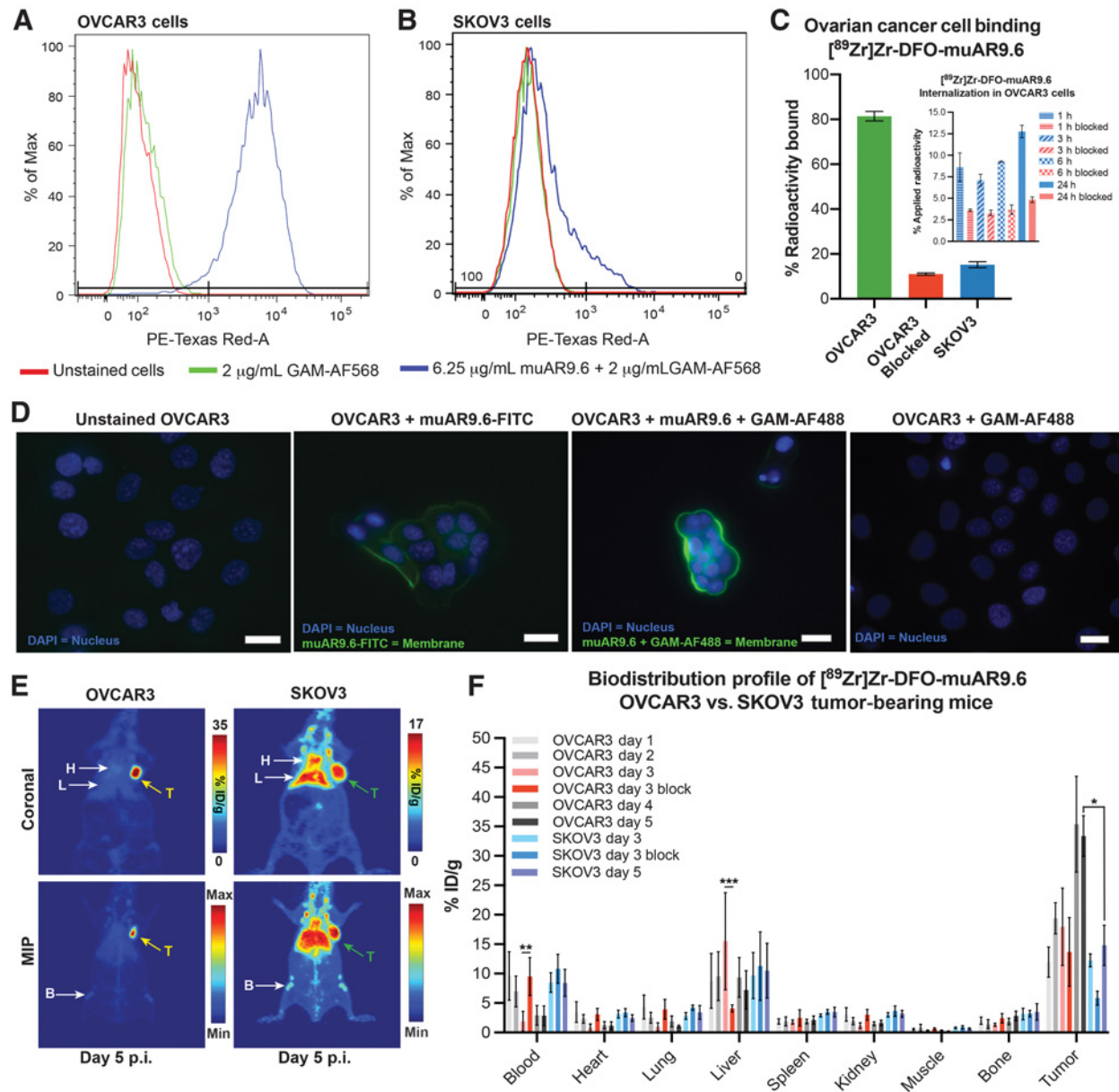


**Figure 1.**

*In vitro* and *in vivo* characterization of the binding of muAR9.6 to ovarian cancer cells. **A** and **B**, Flow cytometry illustrating the strong binding of muAR9.6 to OVCAR3 cells as well as its marginal binding to SKOV3 cells. **C**, RBA showing the high ( $81.4\% \pm 2.1\%$ ) and blockable ( $11\% \pm 1\%$ ) binding of  $^{89}\text{Zr}$ -DFO-muAR9.6 to MUC16-positive OVCAR3 cells as well as its low ( $15.2\% \pm 1.3\%$ ) binding to MUC16-negative SKOV3 cells. The inset shows cellular internalization of  $^{89}\text{Zr}$ -DFO-muAR9.6 between 1 hour and 24 hours after adding to  $\sim 1$  million OVCAR3 cells. The blue bars represent the uptake of 10 ng of  $^{89}\text{Zr}$ -DFO-muAR9.6 at each timepoint, whereas the red bars represent the blocked uptake of  $^{89}\text{Zr}$ -DFO-muAR9.6 in the presence of a 1,000-fold excess of unlabeled muAR9.6. **D**, Immunostaining and fluorescence microscopy of OVCAR3 cells with muAR9.6 and FITC-labeled muAR9.6 revealing the membrane-bound localization of fluorescence. **E**, PET images acquired 5 days after the administration of the  $1.2 \pm 0.1$  mg/kg  $^{89}\text{Zr}$ -DFO-muAR9.6 ( $255 \pm 49.5$   $\mu\text{Ci}$ ;  $9.4 \pm 1.8$  MBq;  $29.6 \pm 2.0$   $\mu\text{g}$ ) in female Nu/Nu mice bearing OVCAR3 and SKOV3 subcutaneous xenografts ( $n = 3$  mice per tumor type). The differential uptake of the radioimmunoconjugate in the tumors (T) can be seen as well as accumulation in other tissue compartments, including the heart [H], liver [L], and bone [B]. The latter is the result of the accretion of free, osteophilic  $^{89}\text{Zr}$ -DFO-muAR9.6 released from the radioimmunoconjugate. Serial PET images are shown in Supplementary Figs. S7 and S8. **F**, *Ex vivo* biodistribution profile up to 5 days after the intravenous administration of  $0.11 \pm 0.02$  mg/kg of  $^{89}\text{Zr}$ -DFO-muAR9.6 ( $24 \pm 1.4$   $\mu\text{Ci}$ ;  $0.88 \pm 0.05$  MBq;  $2.8 \pm 0.5$   $\mu\text{g}$ ) to female Nu/Nu mice bearing OVCAR3 and SKOV3 subcutaneous xenografts ( $n = 5$  mice per tumor type). \*,  $P \leq 0.03$ ; \*\*,  $P \leq 0.01$ ; \*\*\*,  $P \leq 0.0005$ . Detailed sets of %ID/g values are provided in Supplementary Tables S1 and S2. The maximum intensity projections have been scaled from 0% to 100%.



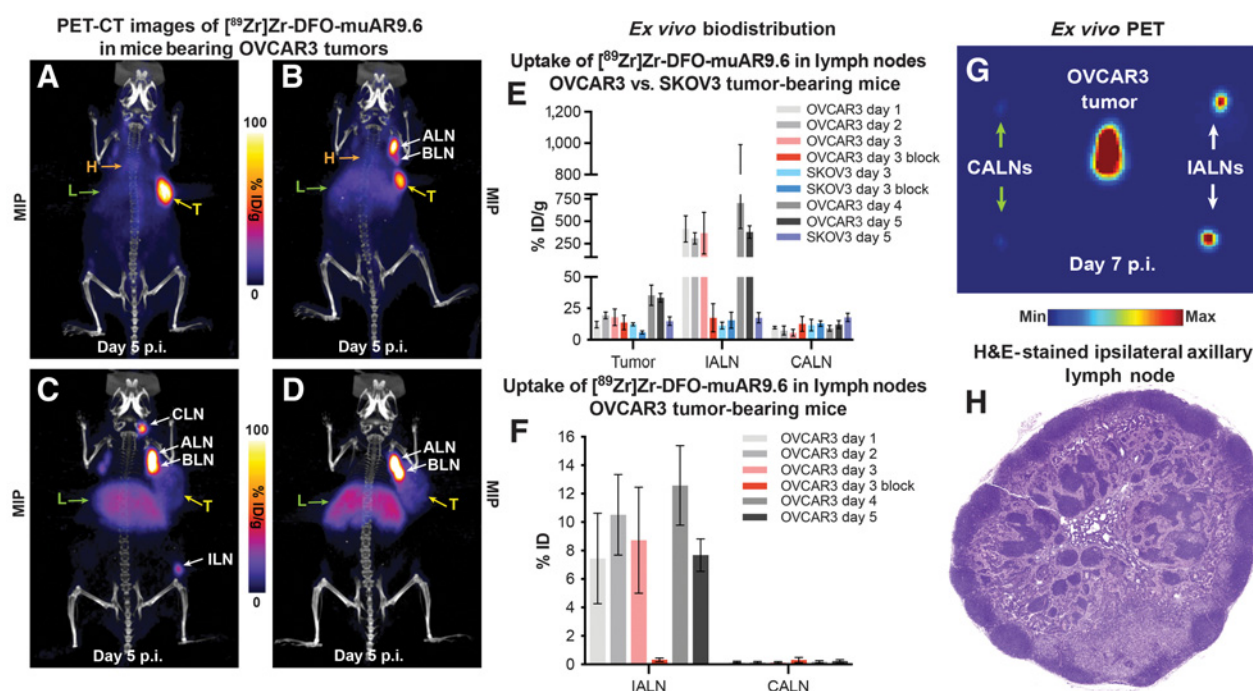
displayed higher radioactivity concentrations in the blood and lower radioactivity concentrations in the liver at 3 d p.i. compared with mice that received the radioimmunoconjugate alone. However, this coinjected unlabeled antibody was not sufficient to significantly block the uptake of [ $^{89}\text{Zr}$ ]Zr-DFO-muAR9.6 at the tumor. The *ex vivo* biodistribution analysis of the mice bearing SKOV3 xenografts yielded predictably straightforward results. In these animals, activity concentrations of  $14.8 \pm 3.4\%$ ID/g,  $10.5 \pm 4.6\%$ ID/g, and  $8.2 \pm 2.8\%$ ID/g were found in the tumor, liver, and blood 5 days after the administration of the radioimmunoconjugate (Fig. 1F; Supplementary Table S2). These data are in agreement with the PET images acquired with [ $^{89}\text{Zr}$ ]Zr-DFO-muAR9.6 in SKOV3-bearing mice (Fig. 1E). Unlike the mice with OVCAR3 xenografts, those bearing SKOV3 xenografts showed no significant heterogeneity in the activity concentrations in the tumor, liver, and blood.

### Lymph node involvement in OVCAR3 xenografts

Additional PET imaging experiments in mice bearing OVCAR3 xenografts lent further insight into the heterogeneity observed in the *ex vivo* biodistribution studies. Tumor-bearing mice with no uptake of [ $^{89}\text{Zr}$ ]Zr-DFO-muAR9.6 in the lymph nodes produced PET images similar to that shown in Fig. 2A. These animals boasted high levels of signal in the subcutaneous tumor with little radioactivity remaining in blood at 5 d p.i. Another subset of

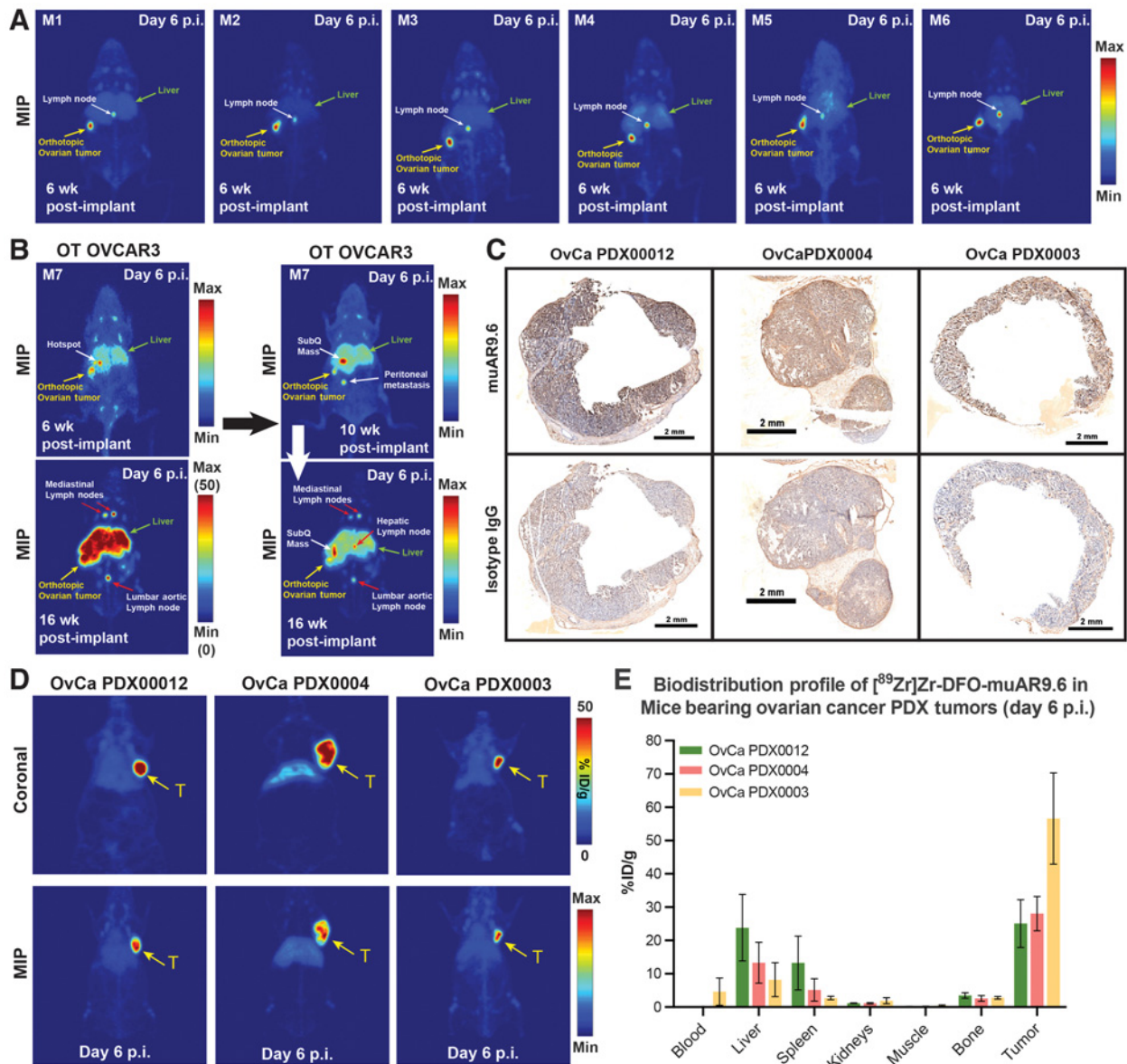
tumor-bearing mice displayed significant radioactivity signal in the ipsilateral lymph node chain paired with relatively low activity concentrations in the tumor and high uptake in the liver (Fig. 2B). This phenomenon was pronounced in mice with relatively larger tumors (Fig. 2C and D; Supplementary Figs. S9 and S10).

A biodistribution analysis confirmed that the uptake of [ $^{89}\text{Zr}$ ]Zr-DFO-muAR9.6 was dramatically higher in the ipsilateral axillary lymph nodes (IALNs) of the OVCAR3-bearing mice compared with the contralateral axillary lymph nodes (CALNs) of the same mice as well as the IALN or CALN of mice bearing SKOV3 xenografts (Fig. 2E; Supplementary Tables S3 and S4). Notably, the coinjection of a 100-fold excess of unlabeled muAR9.6 along with [ $^{89}\text{Zr}$ ]Zr-DFO-muAR9.6 effectively blocked the uptake of radioactivity in the IALNs of mice bearing OVCAR3 xenografts. We plotted the percentage of total injected activity (%ID) in the IALNs and CALNs of the OVCAR3 tumor-bearing mice (Fig. 2F), which provides a more realistic assessment of the uptake of [ $^{89}\text{Zr}$ ]Zr-DFO-muAR9.6 in tiny tissues such as lymph nodes. *Ex vivo* PET imaging corroborated differences in uptake between the IALNs and CALNs of the OVCAR3 tumor-bearing mice (Fig. 2G). Surprisingly, routine histopathologic analysis of PET-positive IALNs did not reveal overt infiltration by neoplastic cells. H&E staining of three-step sections taken 100  $\mu\text{m}$  apart revealed sinus histiocytosis and a moderate number of plasma cells in the



**Figure 2.**

ImmunoPET imaging and *ex vivo* biodistribution data delineate lymph node involvement in mice bearing OVCAR3 xenografts. **A–D**, Maximum intensity projection (MIP) PET-CT images (scaled 0–100) of mice with subcutaneous OVCAR3 xenografts acquired 5 days after the intravenous administration of  $1.2 \pm 0.1$  mg/kg of [ $^{89}\text{Zr}$ ]Zr-DFO-muAR9.6 ( $255 \pm 49.5$   $\mu\text{Ci}$ ;  $9.4 \pm 1.8$  MBq;  $29.6 \pm 2.0$   $\mu\text{g}$ ) showing differing distributions of radioactivity. Heterogeneous patterns of uptake are evident in the tumor (T), lymph nodes (ALN = axillary lymph node; BLN = brachial lymph node; CLN = cervical lymph node; ILN = inguinal lymph node), blood (indicated by the heart, H), and liver (L). **E**, *Ex vivo* biodistribution data comparing the radioactivity concentrations (%ID/g) in the IALNs, CALNs, and subcutaneous tumors of the tumor-bearing mice whose biodistribution data were reported in Fig. 1F. **F**, Graph comparing the percentage of total injected dose (%ID) values for the IALN and CALN at 5 d p.i. in the OVCAR3 tumor-bearing mice whose biodistribution was shown in Fig. 1F. **G**, *Ex vivo* MIP PET image of the tumor, IALNs, and CALNs collected from an OVCAR3-bearing xenograft 7 days after the administration of  $1.2 \pm 0.1$  mg/kg of [ $^{89}\text{Zr}$ ]Zr-DFO-muAR9.6 ( $255 \pm 49.5$   $\mu\text{Ci}$ ;  $9.4 \pm 1.8$  MBq;  $29.6 \pm 2.0$   $\mu\text{g}$ ). **H**, H&E-stained IALN from mouse depicted in Fig. 2D revealing no signs of overt infiltration by neoplastic cells. Detailed sets of %ID/g and %ID values are provided in Supplementary Tables S3 and S4. The maximum intensity projections have been scaled from 0% to 100%.

**Figure 3.**

ImmunoPET delineates the uptake of [<sup>89</sup>Zr]Zr-DFO-muAR9.6 in orthotopic-turned-metastatic and PDX models of HGOC. **A**, PET images (MIPs scaled 0–100) of female nude mice taken 6 weeks after surgical implantation of the left ovary with OVCAR3 cells. ImmunoPET imaging with 1 mg/kg of [<sup>89</sup>Zr]Zr-DFO-muAR9.6 ( $210 \pm 11.7 \mu\text{Ci}$ ;  $7.8 \pm 0.4 \text{ MBq}$ ;  $24 \mu\text{g}$ ) xenografted the orthotopic tumor as well as a lymph node in the hepatic region. **B**, Periodic immunoPET imaging of a murine OVCAR3 xenograft showed disease progression from the primary site of tumor cell inoculation (left ovary) to the liver and distant sites including the mediastinal lymph nodes in the thorax and the lumbar aortic lymph node in the lower abdomen. In this experiment, the mouse was injected three times with [<sup>89</sup>Zr]Zr-DFO-muAR9.6 ( $210 \pm 11.7 \mu\text{Ci}$ ;  $7.8 \pm 0.4 \text{ MBq}$ ;  $24 \mu\text{g}$ ) at 6, 10, and 16 weeks after inoculation, and the images were collected 6 days after each administration of the radioimmunoconjugate. **C**, Cryosections of tumor tissue resected from three human patients with HGOC showing strong immunoreactive staining with muAR9.6 relative to an isotype control IgG used for IHC. **D**, PET images of female NSG mice bearing three different types of subcutaneous PDX (T;  $n = 3$  mice per PDX) injected with 1.3 mg/kg [<sup>89</sup>Zr]Zr-DFO-muAR9.6 ( $248 \pm 5.3 \mu\text{Ci}$ ;  $9.2 \pm 0.2 \text{ MBq}$ ;  $33.0 \pm 4.3 \mu\text{g}$ ). **E**, *Ex vivo* biodistribution data collected 6 days after  $0.12 \pm 0.01 \text{ mg/kg}$  ( $22.7 \pm 1.2 \mu\text{Ci}$ ;  $0.84 \pm 0.04 \text{ MBq}$ ;  $3.0 \pm 0.3 \mu\text{g}$ ) [<sup>89</sup>Zr]Zr-DFO-muAR9.6 was administered intravenously to mice bearing three types of subcutaneous PDX ( $n = 4$  mice per PDX). Detailed %ID/g values are provided in Supplementary Table S5. The maximum intensity projections have been scaled from 0% to 100%.

paracortex and medulla (Fig. 2H; Supplementary Fig. S11). However, the limited sensitivity of H&E does not allow for detection of very small numbers of infiltrating neoplastic cells, especially in tissues with a rather dense and heterogeneous cellularity like the lymph nodes of mice.

#### <sup>89</sup>Zr-AR9.6 immunoPET in clinically relevant tumor models

We next sought to validate the utility of <sup>89</sup>Zr-AR9.6 immunoPET under more clinically relevant conditions. To this end, we developed an orthotopic tumor model by surgically implanting OVCAR3 cells into the bursa of the left ovary of female nude mice. Six weeks after

implanting these cells, immunoPET with [ $^{89}\text{Zr}$ ]Zr-DFO-muAR9.6 delineated both orthotopic tumor tissue and a regional draining lymph node between the liver and the kidneys (Fig. 3A). This phenomenon was observed in eight out of 10 mice bearing orthotopic xenografts used in this study. In some cases, longitudinal PET imaging of these mice allowed us to track disease progression from the initial site of tumor implantation to the infiltration of the liver and metastatic spread to distal lymph nodes (Fig. 3B). Unlike the IALN harvested from mice bearing subcutaneous xenografts, the PET-positive lymph nodes harvested from mice with orthotopic xenografts were effaced by gross infiltration by OVCAR3 tumor cells.

In light of these data, we were curious to explore the binding of muAR9.6 to tumor samples from human patients with ovarian cancer. *Ex vivo* IHC staining of cryosections of tumor samples collected from three patients with high-grade serous ovarian carcinoma yielded IHC positivity by muAR9.6 relative to an isotype control IgG (Fig. 3C).

Encouraged by this result, we then performed *in vivo* immunoPET and *ex vivo* biodistribution studies using female NSG mice bearing subcutaneously implanted PDXs. Both the PET images (Fig. 3D) and the *ex vivo* biodistribution data (Fig. 3E) revealed high uptake of [ $^{89}\text{Zr}$ ]Zr-DFO-muAR9.6 in the tumors—PDX0012 =  $25.1 \pm 7.2\%$  ID/g; PDX0004 =  $28.1 \pm 5.2\%$  ID/g; PDX0003 =  $56.6 \pm 13.7\%$  ID/g—at 6 d p.i. Interestingly, the *ex vivo* biodistribution data uncovered high and heterogeneous concentrations of the radioimmunoconjugate in the livers of the mice bearing each of the three different PDX (PDX0012 =  $23.8 \pm 10.0\%$  ID/g; PDX0004 =  $13.3 \pm 6.1\%$  ID/g; PDX0003 =  $8.2 \pm 5.1\%$  ID/g). The mice bearing PDX0012 also displayed high uptake in the spleen ( $13.2 \pm 8\%$  ID/g) compared with the lower levels of radioactivity in the spleens of the mice with PDX0003 tumors ( $2.7 \pm 0.5\%$  ID/g). Taken together, these data collected using patient samples and PDXs bode well for the future clinical utility of AR9.6 in the context of ovarian cancer.

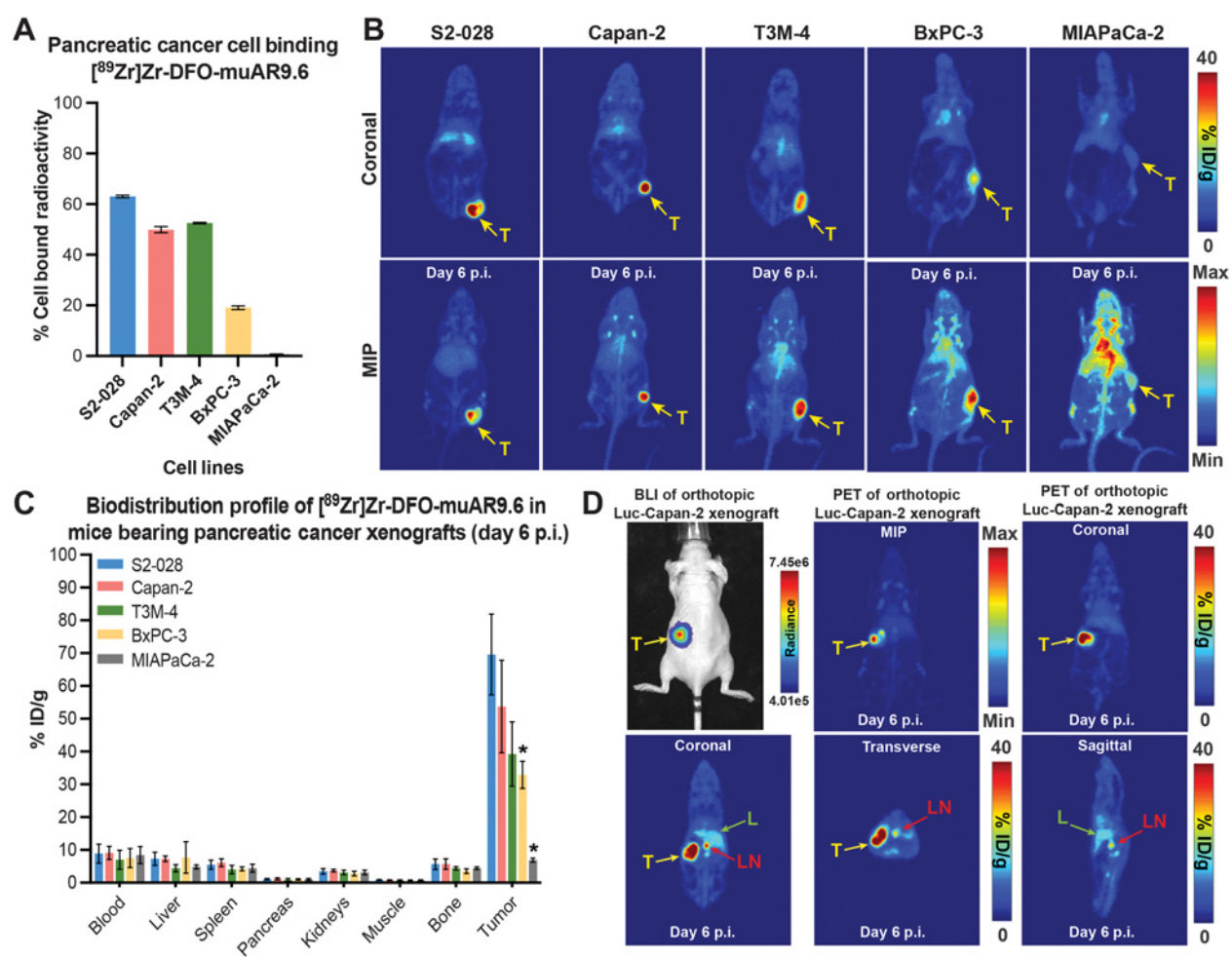


**Figure 4.**

ImmunoPET demonstrates the MUC16-dependent uptake of [ $^{89}\text{Zr}$ ]Zr-DFO-muAR9.6 in xenograft models of pancreatic ductal adenocarcinoma (PDAC). **A**, Graph showing the differential binding of 3 ng of [ $^{89}\text{Zr}$ ]Zr-DFO-muAR9.6 to five PDAC cell lines expressing different levels of MUC16. **B**, PET images of mice bearing subcutaneous PDAC xenografts acquired 6 days after the administration of  $2.1 \pm 0.4$  mg/kg of [ $^{89}\text{Zr}$ ]Zr-DFO-muAR9.6 ( $225 \pm 22.1$   $\mu\text{Ci}$ ;  $8.3 \pm 0.8$  MBq;  $51.7 \pm 9.8$   $\mu\text{g}$ ). **C**, *Ex vivo* biodistribution data acquired from mice bearing subcutaneous PDAC xenografts 6 days after the intravenous injection of  $0.3 \pm 0.03$  mg/kg [ $^{89}\text{Zr}$ ]Zr-DFO-muAR9.6 ( $27.7 \pm 0.9$   $\mu\text{Ci}$ ;  $1.02 \pm 0.03$  MBq;  $6.3 \pm 0.8$   $\mu\text{g}$ ;  $n = 4$  mice per time point). On the graph, \*,  $P \leq 0.05$ . Detailed %ID/g values are provided in Supplementary Table S6. **D**, Representative bioluminescence (BLI) and PET images of female nude mice acquired 4 weeks after the surgical implantation of Luc-Capan-2 cells in the head of the pancreas. The immunoPET images were acquired 6 days after the administration of  $1.57$  mg/kg of [ $^{89}\text{Zr}$ ]Zr-DFO-muAR9.6 ( $269.4 \pm 5.4$   $\mu\text{Ci}$ ;  $9.97 \pm 0.2$  MBq;  $40$   $\mu\text{g}$ ). The maximum intensity projections have been scaled from 0% to 100%.



### Exploring the theranostic utility of AR9.6 for pancreatic cancer

Motivated by our recent reports detailing the mechanism of action and therapeutic utility of muAR9.6 in mouse models of human pancreatic ductal adenocarcinoma (PDAC), we next embarked upon exploring the theranostic utility of this antibody (10). *In vitro* binding of [ $^{89}\text{Zr}$ ]Zr-DFO-muAR9.6 with five pancreatic cancer cell lines—which demonstrated differential expression of MUC16 as determined by Western blot (Supplementary Fig. S3)—showed that the radioimmunoconjugate bound to different cells to different degrees (Fig. 4A). ImmunoPET imaging of nude mice bearing subcutaneous PDAC xenografts corroborated these *in vitro* results (Fig. 4B; Supplementary Fig. S12). Although the mice with S2-028 and Capan-2 xenografts exhibited high tumoral activity concentrations and low levels of radioactivity in the blood at 6 d p.i., those bearing T3M-4 xenografts demonstrated only moderate uptake in the tumor and displayed some persistent radioactivity in the blood at the same time point. Even lower activity concentrations were observed in BxPC-3 xenografts, and the least uptake of all was noted in the MIAPaCa-2 tumors; not surprisingly, mice bearing both types of xenografts exhibited high residual concentrations of [ $^{89}\text{Zr}$ ]Zr-DFO-muAR9.6 in the blood. These imaging data were confirmed by *ex vivo* biodistribution studies of [ $^{89}\text{Zr}$ ]Zr-DFO-muAR9.6 in separate cohorts of mice with subcutaneous PDAC xenografts (Fig. 4C). The S2-028 and Capan-2 xenografts demonstrated high uptake at 6 d p.i. ( $69.5 \pm 12.3$  and  $53.7 \pm 14.1\%$  ID/g, respectively), the T3M-4 and BxPC-3 tumors displayed moderate levels of accumulation ( $39.2 \pm 9.8$  and  $32.9 \pm 4.1\%$  ID/g, respectively), and the MIAPaCa-2 xenografts held the lower activity concentrations of all ( $6.9 \pm 0.6\%$  ID/g). Unlike the PET imaging, however, the biodistribution data did not

uncover significant differences in the activity concentrations in the blood across the various tumor-bearing mice.

These findings in subcutaneous PDAC xenografts were encouraging, so we developed an orthotopic model by surgically implanting luciferase-transfected Capan-2 cells into the head of the pancreas. The mice were monitored weekly via BLI to confirm tumor growth (Fig. 4D). At 4 weeks after surgical implantation, BLI-positive mice were injected with [ $^{89}\text{Zr}$ ]Zr-DFO-muAR9.6 and imaged by PET. Although 15 of 15 mice displayed high activity concentrations in the pancreatic tumor, three exhibited uptake in the adjacent lymph nodes.

### Humanization of muAR9.6 and testing huAR9.6

Murine antibodies present several significant limitations from the standpoint of clinical translation. As a result, we humanized muAR9.6 by germline CDR grafting. Recombinant expression and purification of the humanized variant huAR9.6 yielded up to 60 mg of antibody per liter of ExpiCHO cell culture supernatant (Fig. 5A; Supplementary Figs. S13 and S14). Like its murine predecessor, huAR9.6 was modified with DFO and radiolabeled with [ $^{89}\text{Zr}$ ]Zr $^{4+}$  to produce a radioimmunoconjugate—[ $^{89}\text{Zr}$ ]Zr-DFO-huAR9.6—with high specific activity (10 mCi/mg) and serum stability (Supplementary Figs. S5, S6, and S15). *In vitro* cell binding assay of [ $^{89}\text{Zr}$ ]Zr-labeled huAR9.6 with MUC16<sup>high</sup> OVCAR3 cells demonstrated blockable binding and internalization up to 50% over a 24-hour period (Fig. 5B). Furthermore, *in vitro* flow cytometry analysis with OVCAR3 and SKOV3 cells was performed to functionally validate the antibody. Similar to its murine predecessor, huAR9.6 demonstrated high levels of binding to OVCAR3 cells and only marginal levels of binding to SKOV3 cells (Fig. 5C). Next, we tested the utility of huAR9.6 for *ex vivo* IHC

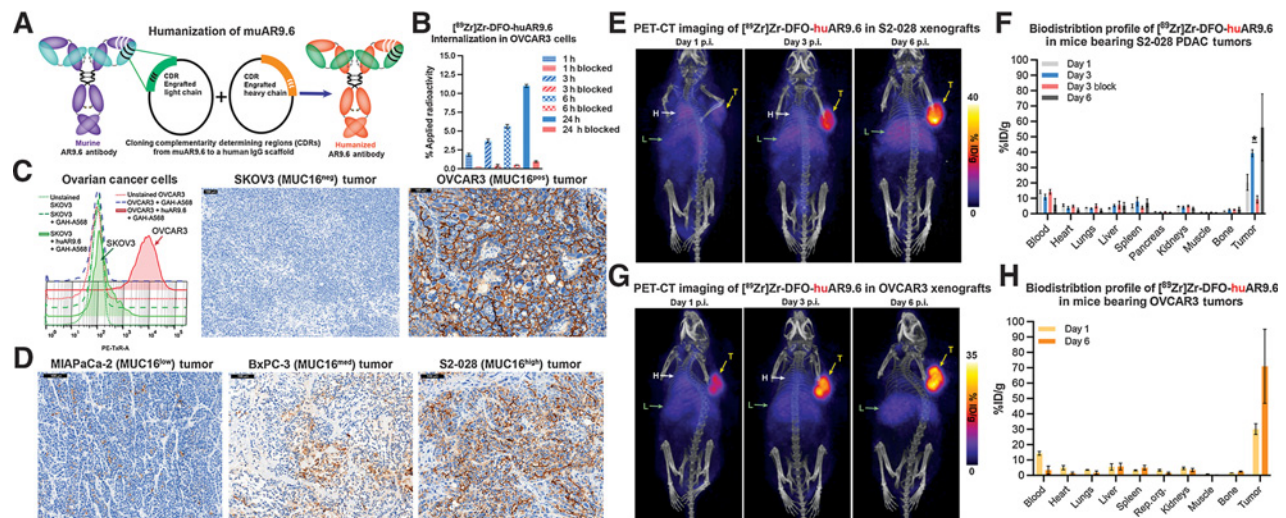


**Figure 5.**

Humanized AR9.6 demonstrates robust *in vitro*, *in vivo*, and *ex vivo* binding to MUC16-expressing ovarian and pancreatic cancer cells. **A**, Humanization of muAR9.6 by CDR grafting. **B**, *In vitro* internalization data of [ $^{89}\text{Zr}$ ]Zr-DFO-huAR9.6 in OVCAR3 cells at 1, 3, 6, and 24 hours. The blue bars represent the uptake of 10 ng of [ $^{89}\text{Zr}$ ]Zr-DFO-huAR9.6 at each timepoint, whereas the red bars represent the blocked uptake of [ $^{89}\text{Zr}$ ]Zr-DFO-huAR9.6 in the presence of a 1,000-fold excess of unlabeled huAR9.6. **C**, *In vitro* and *ex vivo* validation of the binding of huAR9.6 to MUC16<sup>high</sup> (OVCAR3) and MUC16<sup>neg</sup> (SKOV3) ovarian cancer cells using flow cytometry and immunohistochemical (IHC) staining of FFPE tumor sections. **D**, *Ex vivo* validation of the binding of huAR9.6 to FFPE sections from MUC16<sup>high</sup> (S2-028), MUC16<sup>med</sup> (BxPC-3), and MUC16<sup>low</sup> (MIAPaCa-2) tumors. **E** and **G**, Serial PET-CT images of mice bearing subcutaneous S2-028 xenografts (**E**) and OVCAR3 xenografts (**G**;  $n = 3$  mice per tumor xenograft) acquired after the intravenous administration of 2.14 mg/kg [ $^{89}\text{Zr}$ ]Zr-DFO-huAR9.6 (250  $\mu\text{Ci}$ ; 9.25 MBq; 53  $\mu\text{g}$ ) showing gradual accretion of radioactivity in the tumor (T) and the liver (L) as well as gradually declining activity concentrations in the blood (indicated by the heart [H]). **F** and **H**, Longitudinal *ex vivo* biodistribution data acquired after the i.v. injection of 0.25 mg/kg of [ $^{89}\text{Zr}$ ]Zr-DFO-huAR9.6 (29  $\mu\text{Ci}$ ; 1.07 MBq; 6.2  $\mu\text{g}$ ) in mice bearing subcutaneous S2-028 xenografts (**F**) and OVCAR3 xenografts (**H**;  $n = 4$  mice per time point). In the graph shown in **F**,  $P = 0.0286$ . Detailed sets of %ID/g values are provided in Supplementary Tables S7 and S8.



staining of formalin-fixed paraffin-embedded (FFPE) tumor sections from SKOV3 and OVCAR3 tumors. HuAR9.6 showed strong staining of the OVCAR3 tumor compared with the SKOV3 tumor (Fig. 5C). Eager to test huAR9.6 with pancreatic tumors, we tested the antibody for the IHC staining of FFPE sections of S2-028 (MUC16<sup>high</sup>), BxPC-3 (MUC16<sup>med</sup>), and MIAPaCa-2 (MUC16<sup>low</sup>) tumors. HuAR9.6 stained these PDAC sections in a manner consistent with the corresponding *in vitro* and *in vivo* data acquired with its murine predecessor (Fig. 5D).

Finally, we interrogated the *in vivo* performance of [<sup>89</sup>Zr]Zr-DFO-huAR9.6 in mice with subcutaneous pancreatic cancer (S2-028; MUC16<sup>high</sup>) and ovarian cancer (OVCAR3; MUC16<sup>high</sup>) xenografts. Longitudinal PET imaging of the mice bearing S2-028 xenografts demonstrated the gradual accretion of radioactivity in the tumor accompanied by the concomitant clearance of radioactivity from the blood (indicated by the heart), and some uptake of radioactivity in the liver (Fig. 5E). Corresponding *ex vivo* biodistribution data underscored these trends and validated the specificity of [<sup>89</sup>Zr]Zr-DFO-huAR9.6's tumoral uptake via a blockade experiment in which the coinjection of 100-fold excess of unlabeled huAR9.6 blocked the radioactivity concentration in the tumor ( $39.4 \pm 2.3\%$  ID/g vs.  $9.3 \pm 2.3\%$  ID/g;  $P = 0.028$ ) (Fig. 5F).

Longitudinal PET imaging and biodistribution experiments with [<sup>89</sup>Zr]Zr-DFO-huAR9.6 in mice with MUC16-expressing OVCAR3 xenografts produced similarly positive results (Fig. 5G and H). Intriguingly, three of the six mice with OVCAR3 xenografts exhibited uptake of [<sup>89</sup>Zr]Zr-DFO-huAR9.6 along the ipsilateral chain of lymph nodes, a phenomenon previously observed with huAR9.6's murine predecessor (Fig. 6A). This time, however, in addition to performing a coarse analysis of the morphology of PET-positive IALNs by H&E, the granular identification of neoplastic cells was done via IHC. To this end, a pan-cytokeratin (pan-CK) polyclonal antibody (Z0622; Dako)

was used to delineate cytokeratin 7 (CK7) expression by epithelial cells (Fig. 6B–E), whereas huAR9.6 was used to detect cell-associated or soluble MUC16 (Fig. 6F–I). Consistent with our prior experience, morphologic analysis of the H&E-stained sections did not reveal clear tumor cell infiltration of most lymph nodes. However, IHC staining with huAR9.6 showed a diffuse and strong membranous staining of neoplastic cells in the primary tumor and positivity in the cortical sinuses and follicles of PET-positive IALNs (Fig. 6F; Supplementary Figs. S16 and S17). IHC staining with pan-CK and huAR9.6 yielded a strong signal in the primary tumor (Fig. 6B and F), enabled the detection of scattered single neoplastic cells in the subcapsular and subcortical sinuses (Fig. 6C and G), and confirmed the presence of larger metastatic lesions in some PET-positive IALNs (Fig. 6E and I).

In addition to cellular staining, both huAR9.6 and pan-CK IHC yielded non-cell-associated staining patterns. In the vast majority of cases, areas of positivity not clearly associated with a nucleus or with neoplastic cell morphology were detected within different anatomic compartments of the PET-positive IALNs. Widespread and “amorphous” non-cell-associated positive staining was found in the lumen of the subcapsular sinuses. Such a positive signal was interpreted as soluble tumor antigen draining into the node (Fig. 6C). Interestingly, the cellular signal was also observed in the form of a small number of cells in the cortex and paracortex of the lymph node that had a star-shaped morphology similar to dendritic cells or macrophages and displayed moderate to strong, often punctate immunoreactivity, indicative of phagocytized tumor cells or antigen (Fig. 6D and H).

## Discussion

The therapeutic mechanism of muAR9.6 distinguishes it from other MUC16-targeted antibodies, including those reported from our

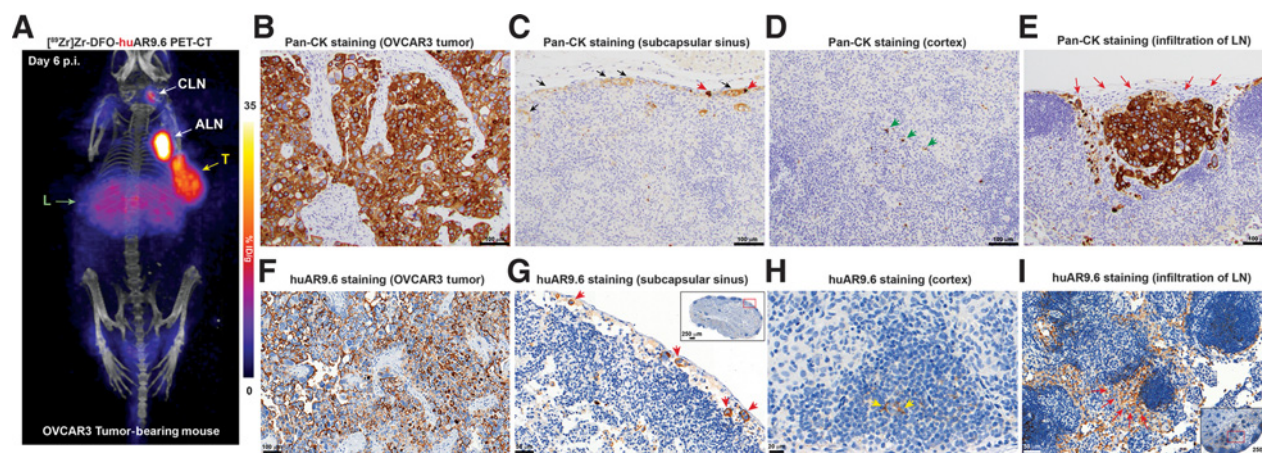


**Figure 6.**

huAR9.6 can delineate lymph node involvement in a xenograft model of ovarian cancer. **A**, PET-CT image of a mouse bearing a subcutaneous OVCAR3 xenograft acquired 6 days after the intravenous injection of 2.14 mg/kg [<sup>89</sup>Zr]Zr-DFO-huAR9.6 (250  $\mu$ Ci; 9.25 MBq; 53  $\mu$ g) showing uptake of radioactivity in the tumor (T), liver (L), and ipsilateral lymph node chain. **B**, Pan-cytokeratin (pan-CK) IHC staining of the OVCAR3 tumor showing a pattern of CK expression that is characteristic of epithelial cancer cells. **C–E**, Pan-CK IHC staining of the PET-positive IALN showing (C) immunoreactive foci of neoplastic cells (red arrowheads) and lymphatic fluid (black arrows) in the subcapsular sinuses. **D**, The cortex of the LN showing CK positivity in star-shaped cells (green arrowheads) indicative of dendritic cells and (E) a cluster of neoplastic cells infiltrating the IALN (red arrows) (E); **F**, IHC staining of the OVCAR3 tumor with huAR9.6 showing membranous staining of the OVCAR3 cells. **G–I**, huAR9.6 IHC staining of the PET-positive IALN (G) showing the presence of a few neoplastic cells (red arrowheads). The inset shows the appearance of the huAR9.6-stained PET-positive but H&E-negative IALN, and the red box in the inset identifies the portion shown in the main image. **H**, The cortex and follicles of the LN showing positivity for huAR9.6 staining in star-shaped cells (yellow arrowheads) indicative of dendritic cells. **I**, A cluster of neoplastic cells draining into and infiltrating the medulla of the IALN (red arrows). The inset shows the architecture and appearance of the corresponding huAR9.6-stained PET-positive but H&E-negative IALN, and the red box in the inset identifies the portion shown in the main image.

laboratories (10, 13, 15, 16, 24, 25, 31, 32). Motivated by its novelty, we set out to validate the *in vitro* cell binding of muAR9.6 and explore the *in vivo* behavior of a  $^{89}\text{Zr}$ -labeled variant of the antibody in preclinical tumor models. Flow cytometry revealed strong binding of muAR9.6 to MUC16-positive OVCAR3 cells as well as—more surprisingly—some binding to SKOV3 cells. The latter are considered MUC16 negative, and we have previously not observed binding of other MUC16-targeting antibodies such as B43.13 and 4H11 to SKOV3 cells (24, 25, 33, 34). However, Reinartz and colleagues have shown that SKOV3 cells have very low levels of MUC16 transcript (mRNA), and although they reported no binding of anti-CA125 antibodies to SKOV3 cells, Felder and colleagues reported marginal binding of OC125-like MUC16-binding antibodies to SKOV3 cells via flow cytometry. Plausibly, alternative splicing or posttranslational modifications may be causing the AR9.6 epitope to be expressed on SKOV3 cells, leading to marginal binding to this cell line that is otherwise considered MUC16 negative (14, 32). In our hands, using muAR9.6 as the primary antibody for Western blotting of SKOV3 cell lysate revealed binding of the antibody to a low-molecular-weight band observed in the other MUC16-positive cell lines such as OVCAR3, Capan-2, S2-2028, and T3M-4 (Supplementary Fig. S3). The latter band may represent an isoform/splice variant or truncated version of the MUC16 epitope expressed by SKOV3 cells. The specificity of muAR9.6's binding to OVCAR3 cells was further demonstrated via radioligand binding assays, and fluorescence microscopy experiments revealed that both unmodified muAR9.6 and an FITC-labeled variant produced membrane-bound fluorescence with OVCAR3 cells (Fig. 1D). The latter data are consistent with MUC16 being a membrane-anchored glycoprotein and are in line with our prior findings with B43.13, a clinically relevant MUC16-targeted antibody (26).

Shifting gears to the *in vivo* experiments, the differing radioactivity concentrations of  $^{89}\text{Zr}$ -DFO-muAR9.6 observed in the OVCAR3 and SKOV3 tumors were consistent with the *in vitro* binding of the antibody to these two cell types. Unlike other MUC16-targeting antibodies such as B43.13 or 4H11 that have demonstrated potential theranostic utility in the setting of high-grade serous ovarian carcinoma, the ability of AR9.6 to delineate SKOV3 tumors extends its utility for the noninvasive imaging and targeted therapy of clear cell carcinoma of the ovaries. Notably, the imaging and *ex vivo* biodistribution experiments in the OVCAR3 tumor-bearing mice proved particularly interesting, as they highlighted the influence that the lymphatic and reticuloendothelial systems have on the performance of radioimmunoconjugates that target shed antigens like MUC16. With respect to the former, the root cause of the accretion of  $^{89}\text{Zr}$ -DFO-muAR9.6 in the lymph nodes ipsilateral to the tumor demanded interrogation. The histologic examination of these PET-positive IALNs did not show overt infiltration by tumor cells. Yet MUC16 is a shed antigen, and the epitope to which muAR9.6 binds lies in the portion of the cleaved antigen. As a result, it is likely that the lymph nodes along the ipsilateral chain could accumulate reservoirs of the shed antigen and thus sequester  $^{89}\text{Zr}$ -DFO-muAR9.6. The uptake of  $^{89}\text{Zr}$ -DFO-muAR9.6 in the IALN could be blocked in mice that were coinjected with 100-fold excess of unlabeled muAR9.6, a result that confirms the role of target binding in this accretion. We previously observed a similar behavior with  $^{89}\text{Zr}$ -DFO-5B1, a radioimmunoconjugate that targets another shed antigen: CA19-9. In this case, predosing animals with unlabeled parent mAb prior to the injection of the  $^{89}\text{Zr}$ -radioimmunoconjugate mitigated lymph node uptake and increased tumoral activity concentrations (35).

The heterogeneity of the uptake of  $^{89}\text{Zr}$ -DFO-muAR9.6 in the livers of the OVCAR3-bearing mice may also stem from the shedding of MUC16 and the clearance of circulating radioimmunocomplexes by the reticuloendothelial system (RES). Other MUC16-targeting antibodies such as B43.13 have been shown to form immunocomplexes with soluble MUC16 in the serum of patients with ovarian cancer (36, 37), and the majority of these immunocomplexes have been shown to sequester within 30 minutes p.i. in the RES (*i.e.*, liver). Indeed, in this study, we noted higher activity concentrations in the IALNs and livers of mice bearing larger OVCAR3 xenografts, which may shed higher titers of MUC16 into the blood and lymph. Taken together, these data plainly illustrate that while the shedding of MUC16 does not preclude the use of  $^{89}\text{Zr}$ -DFO-muAR9.6 for effective tumor imaging, it does mean that care will need to be taken to optimize the dose and specific activity of the radioimmunoconjugate in the clinical setting. Doing so will minimize false positives in the lymph nodes and reduce the buildup of signal in the liver while simultaneously maximizing uptake in tumor tissue.

The role of MUC16 in the progression and metastasis of PDAC fueled our evaluation of  $^{89}\text{Zr}$ -DFO-muAR9.6 in five subcutaneous xenograft models and one orthotopic xenograft model of pancreatic cancer (9, 10). These results were particularly compelling, as the differential tumor uptake of the radioimmunoconjugate in these preclinical models of PDAC suggests that  $^{89}\text{Zr}$ -AR9.6 immunoPET could be used to facilitate patient selection for treatment with AR9.6. Furthermore, these imaging data, the established efficacy of combination therapy with muAR9.6 and gemcitabine in preclinical models of PDAC, and gemcitabine's properties as a radiosensitizer suggest that muAR9.6 may have promise as a vector for the radioimmunotherapy of MUC16-positive PDAC either alone or in combination with gemcitabine (38). Finally, because muAR9.6 is cross-reactive with murine MUC16, it may also be possible to use syngeneic mouse models of PDAC to carry out proof-of-concept studies that combine muAR9.6 with emerging immune-checkpoint inhibitors in pursuit of effective immunotherapies for the disease (39, 40).

The final stage of the current investigation was centered on the creation and validation of huAR9.6, the humanized—and thus more readily translated—variant of muAR9.6. The excellent *in vitro*, *ex vivo*, and *in vivo* target-binding ability of huAR9.6 is a testament to the advances in recombinant DNA technology and protein expression that allow for the humanization of murine monoclonal antibodies (41). Importantly, immunoPET with  $^{89}\text{Zr}$ -DFO-huAR9.6 in mice bearing MUC16-positive OVCAR3 xenografts produced images similar to those acquired with the murine variant of the antibody. This time, however, histopathologic findings from PET-positive IALNs suggested three distinct mechanisms behind the accumulation of  $^{89}\text{Zr}$ -DFO-huAR9.6 in these tissues. The first and simplest explanation is predicated on the shedding of the extracellular domain of MUC16 from the primary OVCAR3 tumor to the IALNs. Mucins such as MUC16 have been shown to interact with immune cells to create an immunosuppressive microenvironment that facilitates metastasis (42, 43). That the pan-CK staining of lymphatic fluid was predominantly noncellular with only occasional positive cells in the subcapsular sinuses of the PET-positive lymph nodes is suggestive of the accumulation of shed antigen and cell debris in the IALNs. The sparsely distributed, pan-CK-positive star-shaped cells in the paracortex of the PET-positive IALNs hold the key to the second mechanism. These cells, we hypothesize, may represent phagocytized infiltrating neoplastic cells. That some of these cells could be stained with huAR9.6 during IHC suggests that the target antigen (*i.e.*, MUC16) could be presented on the surface of

dendritic cells or macrophages, another possible sink for [ $^{89}\text{Zr}$ ]Zr-DFO-huAR9.6 in the PET-positive IALNs. The third—and probably most likely—possible explanation is the metastasis of OVCAR3 cells from the primary tumor to the draining lymph nodes. This scenario is consistent with clinical data, as ovarian cancer is known to spread via the retroperitoneal lymphatics (among other routes), and MUC16-positive serous adenocarcinomas are reported to have a higher propensity for metastases to lymph nodes (44–46).

Questions of mechanism aside, the PET data clearly underscore the sensitivity of [ $^{89}\text{Zr}$ ]Zr-DFO-huAR9.6 immunoPET for the noninvasive delineation of draining, immunoreactive, and metastatic lymph nodes. Systematic lymphadenectomy is typically unwarranted during cytoreductive surgery of patients with ovarian cancer who have undergone neoadjuvant chemotherapy (47). However, because ovarian cancer—and pancreatic cancer, for that matter—is a surgically treated disease, the noninvasive, preoperative delineation of draining or metastatic LNs can provide a road map for surgeons to selectively resect PET-positive LNs while leaving minimal residual disease behind and avoiding morbidities associated with extensive lymphadenectomies.

## Conclusion

Herein, we report the *in vitro*, *ex vivo*, and *in vivo* validation of a pair of radioimmunoconjugates—[ $^{89}\text{Zr}$ ]Zr-DFO-muAR9.6 and [ $^{89}\text{Zr}$ ]Zr-DFO-huAR9.6—based on the novel MUC16-targeted therapeutic mAb AR9.6. AR9.6's unique mechanism of action, favorable *in vivo* pharmacokinetic profile, and availability as a humanized variant combine to give the antibody clinical promise as both a therapeutic and a platform for theranostic PET imaging in MUC16-positive ovarian and pancreatic cancer.

## Authors' Disclosures

C.L. Brooks reports grants from Quest PharmaTech Inc. during the conduct of the study and grants from Quest PharmaTech Inc. outside the submitted work. R. Madiyalakan reports personal fees from Quest PharmaTech Inc during the conduct of the study; personal fees from OncoQuest Inc outside the submitted work; and has a patent 17048119 pending to Quest PharmaTech. M.A. Hollingsworth reports grants from the NCI during the conduct of the study; other support from OncoCare Therapeutics outside the submitted work; and has a patent 62669058 issued. P. Radhakrishnan reports grants from the NCI during the conduct of the study; other support from OncoCare Therapeutics outside the submitted work; and has a patent 62669058 issued. J.S. Lewis reports grants from NIH, Emerson

Collective Cancer Research Fund, William H. Goodwin and Mrs. Alice Goodwin and the Commonwealth Foundation for Cancer Research, Tow Foundation, and IMRAS MSKCC during the conduct of the study. No disclosures were reported by the other authors.

## Authors' Contributions

**S.K. Sharma:** Conceptualization, validation, investigation, visualization, methodology, writing—original draft, writing—review and editing. **K.N. Mack:** Investigation, visualization, and methodology. **A. Piersigilli:** Investigation, visualization, and methodology. **J. Pourat:** Investigation, visualization, and methodology. **K.J. Edwards:** Investigation, visualization, and methodology. **O. Keinänen:** Investigation and methodology. **M.S. Jiao:** Investigation, visualization, and methodology. **H. Zhao:** Investigation, visualization, and methodology. **B. White:** Investigation and methodology. **C.L. Brooks:** Investigation and methodology. **E. de Stanchina:** Investigation and methodology. **M.R. Madiyalakan:** Resources and investigation. **M.A. Hollingsworth:** Resources, investigation, and methodology. **P. Radhakrishnan:** Resources and investigation. **J.S. Lewis:** Conceptualization, supervision, funding acquisition, project administration, writing—review and editing. **B.M. Zeglis:** Conceptualization, resources, supervision, funding acquisition, methodology, writing—original draft, project administration, writing—review and editing.

## Acknowledgments

We gratefully acknowledge Dr. Sebastien Monette for help with *ex vivo* histopathologic examination and Dr. Eric E. Gardner for providing the luciferase-transfected Capan-2 cell line that was used for the development of the orthotopic pancreatic cancer xenograft model. This work was supported by the MSKCC Small Animal Imaging Core Facility (funded in part by the NIH Small-Animal Imaging Research Program Grant R24 CA83084 and NIH Center Grant P30 CA08748) as well as the Radiochemistry and Molecular Imaging Probe core and the Tri-Institutional Laboratory of Comparative Pathology, which are also funded in part by NIH grant P30 CA08748. This work was also supported by the funds awarded to J.S. Lewis from the NIH (R35CA232130), the Emerson Collective Cancer Research Fund, the Mr. William H. Goodwin and Mrs. Alice Goodwin and the Commonwealth Foundation for Cancer Research and The Center for Experimental Therapeutics at Memorial Sloan Kettering Cancer Center. S.K. Sharma acknowledges the Tow Foundation for a Postdoctoral Fellowship Award and funding to support this work. B.M. Zeglis, C.L. Brooks, P. Radhakrishnan, and M.A. Hollingsworth also acknowledge the NIH for support (B.M. Zeglis: R01CA240963, U01CA221046, R01CA204167, R21EB030275, and R01CA244327; C.L. Brooks: R15CA242349; P. Radhakrishnan and M.A. Hollingsworth: CA208108, P01CA217798, and U01CA237629).

The costs of publication of this article were defrayed in part by the payment of page charges. This article must therefore be hereby marked *advertisement* in accordance with 18 U.S.C. Section 1734 solely to indicate this fact.

Received May 17, 2021; revised August 17, 2021; accepted December 8, 2021; published first December 13, 2021.

## References

1. Siegel RL, Miller KD, Jemal A. Cancer statistics, 2020. *CA Cancer J Clin* 2020;70:7–30.
2. Strobel O, Neoptolemos J, Jager D, Buchler MW. Optimizing the outcomes of pancreatic cancer surgery. *Nat Rev Clin Oncol* 2019;16:11–26.
3. Nishio S, Ushijima K. Clinical significance of primary debulking surgery and neoadjuvant chemotherapy-interval debulking surgery in advanced ovarian cancer. *Jpn J Clin Oncol* 2020;50:379–86.
4. Thomas D, Rathinavel AK, Radhakrishnan P. Altered glycosylation in cancer: a promising target for biomarkers and therapeutics. *Biochim Biophys Acta Rev Cancer* 2021;1875:188464.
5. Hollingsworth MA, Swanson BJ. Mucins in cancer: protection and control of the cell surface. *Nat Rev Cancer* 2004;4:45–60.
6. Radhakrishnan P, Dabelsteen S, Madsen FB, Francavilla C, Kopp KL, Steentoft C, et al. Immature truncated O-glycophenotype of cancer directly induces oncogenic features. *Proc Natl Acad Sci U S A* 2014;111:E4066–75.
7. Ju T, Aryal RP, Kudelka MR, Wang Y, Cummings RD. The Cosmc connection to the Tn antigen in cancer. *Cancer Biomark* 2014;14:63–81.
8. Gupta D, Lis CG. Role of CA125 in predicting ovarian cancer survival – a review of the epidemiological literature. *J Ovarian Res* 2009;2:13.
9. Haridas D, Chakraborty S, Ponnusamy MP, Lakshmanan I, Rachagani S, Cruz E, et al. Pathobiological implications of MUC16 expression in pancreatic cancer. *PLoS One* 2011;6:e26839.
10. Thomas D, Sagar S, Liu X, Lee HR, Grunkemeyer JA, Grandgenett PM, et al. Isoforms of MUC16 activate oncogenic signaling through EGF receptors to enhance the progression of pancreatic cancer. *Mol Ther* 2021;29:1557–71.
11. Aithal A, Rauth S, Kshirsagar P, Shah A, Lakshmanan I, Junker WM, et al. MUC16 as a novel target for cancer therapy. *Expert Opin Ther Targets* 2018;22:675–86.
12. Chen Y, Clark S, Wong T, Chen Y, Chen Y, Dennis MS, et al. Armed antibodies targeting the mucin repeats of the ovarian cancer antigen, MUC16, are highly efficacious in animal tumor models. *Cancer Res* 2007;67:4924–32.
13. Crawford A, Haber L, Kelly MP, Vazzana K, Canova L, Ram P, et al. A Mucin 16 bispecific T cell-engaging antibody for the treatment of ovarian cancer. *Sci Transl Med* 2019;11:eau7534.



14. Felder M, Kapur A, Gonzalez-Bosquet J, Horibata S, Heintz J, Albrecht R, et al. MUC16 (CA125): tumor biomarker to cancer therapy, a work in progress. *Mol Cancer* 2014;13:129.
15. Rao TD, Fernandez-Tejada A, Axelrod A, Rosales N, Yan X, Thapi S, et al. Antibodies against specific MUC16 glycosylation sites inhibit ovarian cancer growth. *ACS Chem Biol* 2017;12:2085–96.
16. Schultes BC, Zhang C, Xue LY, Noujaim AA, Madiyalakan R. Immunotherapy of human ovarian carcinoma with OvaRex MAb-B43.13 in a human-PBL-SCID/BG mouse model. *Hybridoma* 1999;18:47–55.
17. Li T, Wang J. Therapeutic effect of dual CAR-T targeting PDL1 and MUC16 antigens on ovarian cancer cells in mice. *BMC Cancer* 2020;20:678.
18. Yeku OO, Purdon TJ, Koneru M, Spriggs D, Brentjens RJ. Armored CAR T cells enhance antitumor efficacy and overcome the tumor microenvironment. *Sci Rep* 2017;7:10541.
19. Koneru M, O'Cearbhaill R, Pendharkar S, Spriggs DR, Brentjens RJ. A phase I clinical trial of adoptive T cell therapy using IL-12 secreting MUC-16(ecto) directed chimeric antigen receptors for recurrent ovarian cancer. *J Transl Med* 2015;13:102.
20. Marcos-Silva L, Narimatsu Y, Halim A, Campos D, Yang Z, Tarp MA, et al. Characterization of binding epitopes of CA125 monoclonal antibodies. *J Proteome Res* 2014;13:3349–59.
21. Aithal A, Junker WM, Kshirsagar P, Das S, Kaur S, Orzechowski C, et al. Development and characterization of carboxy-terminus specific monoclonal antibodies for understanding MUC16 cleavage in human ovarian cancer. *PLoS One* 2018;13:e0193907.
22. Dharma Rao T, Park KJ, Smith-Jones P, Iasonos A, Linkov I, Soslow RA, et al. Novel monoclonal antibodies against the proximal (carboxy-terminal) portions of MUC16. *Appl Immunohistochem Mol Morphol* 2010;18:462–72.
23. Fung K, Sharma SK, Keinänen O, Roche KL, Lewis JS, Zeglis BM. A molecularly targeted intraoperative near-infrared fluorescence imaging agent for high-grade serous ovarian cancer. *Mol Pharm* 2020;17:3140–7.
24. Nemieboka B, Sharma SK, Rao TD, Edwards KJ, Yan S, Wang P, et al. Radiopharmacologic screening of antibodies to the unshed ectodomain of MUC16 in ovarian cancer identifies a lead candidate for clinical translation. *Nucl Med Biol* 2020;86–87:9–19.
25. Sharma SK, Sevak KK, Monette S, Carlin SD, Knight JC, Wuest FR, et al. Preclinical 89Zr immuno-PET of high-grade serous ovarian cancer and lymph node metastasis. *J Nucl Med* 2016;57:771–6.
26. Sharma SK, Wuest M, Wang M, Glubrecht D, Andrais B, Lapi SE, et al. Immuno-PET of epithelial ovarian cancer: harnessing the potential of CA125 for non-invasive imaging. *EJNMMI Res* 2014;4:60.
27. Vosjan MJ, Perk LR, Visser GW, Budde M, Jurek P, Kiefer GE, et al. Conjugation and radiolabeling of monoclonal antibodies with zirconium-89 for PET imaging using the bifunctional chelate p-isothiocyanatobenzyl-desferrioxamine. *Nat Protoc* 2010;5:739–43.
28. Mattar M, McCarthy CR, Kulick AR, Qeriqi B, Guzman S, de Stanchina E. Establishing and maintaining an extensive library of patient-derived xenograft models. *Front Oncol* 2018;8:19.
29. Kim MP, Evans DB, Wang H, Abbruzzese JL, Fleming JB, Gallick GE. Generation of orthotopic and heterotopic human pancreatic cancer xenografts in immunodeficient mice. *Nat Protoc* 2009;4:1670–80.
30. Hwang WY, Almagro JC, Buss TN, Tan P, Foote J. Use of human germline genes in a CDR homology-based approach to antibody humanization. *Methods* 2005;36:35–42.
31. Noujaim AA, Schultes BC, Baum RP, Madiyalakan R. Induction of CA125-specific B and T cell responses in patients injected with MAb-B43.13—evidence for antibody-mediated antigen-processing and presentation of CA125 in vivo. *Cancer Biother Radiopharm* 2001;16:187–203.
32. Stasencko M, Smith E, Yeku O, Park KJ, Laster I, Lee K, et al. Targeting galectin-3 with a high-affinity antibody for inhibition of high-grade serous ovarian cancer and other MUC16/CA-125-expressing malignancies. *Sci Rep* 2021;11:3718.
33. Boivin M, Lane D, Piche A, Rancourt C. CA125 (MUC16) tumor antigen selectively modulates the sensitivity of ovarian cancer cells to genotoxic drug-induced apoptosis. *Gynecol Oncol* 2009;115:407–13.
34. Reinartz S, Failer S, Schuell T, Wagner U. CA125 (MUC16) gene silencing suppresses growth properties of ovarian and breast cancer cells. *Eur J Cancer* 2012;48:1558–69.
35. Houghton JL, Abdel-Atti D, Scholz WW, Lewis JS. Preloading with unlabeled CA19.9 targeted human monoclonal antibody leads to improved PET imaging with (89)Zr-5B1. *Mol Pharm* 2017;14:908–15.
36. McQuarrie SA, Baum RP, Niesen A, Madiyalakan R, Korz W, Sykes TR, et al. Pharmacokinetics and radiation dosimetry of 99Tcm-labelled monoclonal antibody B43.13 in ovarian cancer patients. *Nucl Med Commun* 1997;18:878–86.
37. McQuarrie SA, Riauka T, Baum RP, Sykes TR, Noujaim AA, Boniface G, et al. The effects of circulating antigen on the pharmacokinetics and radioimmunoscintigraphic properties of 99m Tc labelled monoclonal antibodies in cancer patients. *J Pharm Sci* 1998;1:115–25.
38. Lawrence TS, Eisbruch A, Shewach DS. Gemcitabine-mediated radiosensitization. *Semin Oncol* 1997;24:S7–24–S7–8.
39. Palaia I, Tomao F, Sassu CM, Musacchio L, Benedetti Panici P. Immunotherapy for ovarian cancer: recent advances and combination therapeutic approaches. *Oncotargets Ther* 2020;13:6109–29.
40. Christenson ES, Jaffee E, Azad NS. Current and emerging therapies for patients with advanced pancreatic ductal adenocarcinoma: a bright future. *Lancet Oncol* 2020;21:e135–e45.
41. Kuramochi T, Igawa T, Tsunoda H, Hattori K. Humanization and simultaneous optimization of monoclonal antibody. *Methods Mol Biol* 2019;1904:213–30.
42. Belisle JA, Horibata S, Jennifer GA, Petrie S, Kapur A, Andre S, et al. Identification of Siglec-9 as the receptor for MUC16 on human NK cells, B cells, and monocytes. *Mol Cancer* 2010;9:118.
43. Bhatia R, Gautam SK, Cannon A, Thompson C, Hall BR, Aithal A, et al. Cancer-associated mucins: role in immune modulation and metastasis. *Cancer Metastasis Rev* 2019;38:223–36.
44. Berek JS. Lymph node-positive stage IIIC ovarian cancer: a separate entity? *Int J Gynecol Cancer* 2009;19:S18–20.
45. Di Re F, Baiocchi G. Value of lymph node assessment in ovarian cancer: Status of the art at the end of the second millennium. *Int J Gynecol Cancer* 2000;10:435–42.
46. Haller H, Mamula O, Krasevic M, Rupic S, Fischer AB, Eminovic S, et al. Frequency and distribution of lymph node metastases in epithelial ovarian cancer. *Int J Gynecol Cancer* 2011;21:245–50.
47. Lin Q, Liu W, Xu S, Li J, Tong J. The value of systematic lymphadenectomy during debulking surgery in the treatment of ovarian cancer: a meta-analysis of randomized controlled trials. *J Ovarian Res* 2020;13:56.